applied optics

High-accuracy spectral reduction algorithm for the échelle spectrometer

Lu Yin, Bayanheshig,* Jin Yang, Yuxian Lu, Rui Zhang, Ci Sun, and Jicheng Cui

Grating Technology Laboratory, Changchun Institute of Optics and Fine Mechanics and Physics, Chinese Academy of Sciences, Changchun, Jilin 130033, China

*Corresponding author: bayin888@sina.com

Received 27 January 2016; revised 8 April 2016; accepted 8 April 2016; posted 8 April 2016 (Doc. ID 258396); published 27 April 2016

A spectral reduction algorithm for an échelle spectrometer with spherical mirrors that builds a one-to-one correspondence between the wavelength and pixel position is proposed. The algorithm accuracy is improved by calculating the offset distance of the principal ray from the center of the image plane in the two-dimensional vertical direction and compensating the spectral line bending from the reflecting prism. The simulation and experimental results verify that the maximum deviation of the entire image plane is less than one pixel. This algorithm ensures that the wavelengths calculated from spectrograms have a high spectral resolution, meaning the precision from the spectral analysis reaches engineering standards of practice.

OCIS codes: (050.0050) Diffraction and gratings; (120.0120) Instrumentation, measurement, and metrology; (120.4640) Optical instruments.

http://dx.doi.org/10.1364/AO.55.003574

1. INTRODUCTION

With their high resolution, small size, full-spectrum direct reading, wide band, and many other advantages [1–7], échelle spectrometers are becoming popular spectrometric instruments of choice. Their high-resolution feature, which is the most important, requires a highly accurate spectral reduction algorithm [2]. Nevertheless, developing algorithms and error compensation for the échelle spectrometer have proved difficult and important problems. A spectral reduction algorithm is designed to perform an analysis to extract the relationship between the pixel position on the image plane and its wavelength.

By investigating in detail the workings of the échelle spectrometer [8], many studies have produced a series of methods to obtain this relationship. Initially, ray-tracing methods [9] were widely used, as all wavelengths covering the spectral range were considered and their positions on the image plane were calculated by geometrical optic rules. While choosing a large wavelength interval does not characterize the relationship in detail, choosing a small wavelength interval requires a very large amount of computation. Later, more simplified algorithms were proposed, the main idea being to use several monochromatic light rays to determine the position of the reference point and then use mathematical methods (such as interpolation and fitting) to evaluate the relationship of the entire image plane [10,11]. Such methods greatly enhanced the speed of algorithms, but failed to achieve the required accuracy. References [12,13] proposed a spectral reduction algorithm by establishing a function [14] depending on the wavelength and pixel position. A simplified optical model was established to calculate the correspondence between the wavelength and pixel position. The offset distance from the center of the image plane is calculated by using the equivalent deflection angle, which is considered equal to the offset angle from the principal ray. Although this simplified model further improved speed and accuracy, it is only suitable for an échelle spectrometer with an off-axis parabolic mirror. When using a spherical mirror instead of an off-axis parabolic mirror or an asymmetrical structure, the model error increased significantly.

As an échelle spectrometer with an off-axis parabolic mirror has high processing costs and is difficult to adjust, it is necessary to reassess the spectral reduction algorithm for an échelle spectrometer with spherical mirrors. In Ref. [13], the authors rethought the calculation of the offset distance in the two-dimensional vertical direction of a CCD image plane. The method combines a functional treatment [14] with the ray-tracing technique, which has high accuracy. Using the analysis from geometric optics, the light path is considered in greater detail without simplification, where the spectral line bending of the reflecting prism is taken into consideration to compensate for the algorithm's error. The accuracy of the spectral reduction algorithm is then significantly improved without sacrificing calculation speed. The algorithm error over the entire image plane is less than one pixel, an accuracy that is essential for high-spectral-resolution instruments.

2. THEORY OF THE ÉCHELLE SPECTROMETER

The spectral reduction algorithm described below is suitable for an échelle spectrometer (Fig. 1) with spherical mirrors.

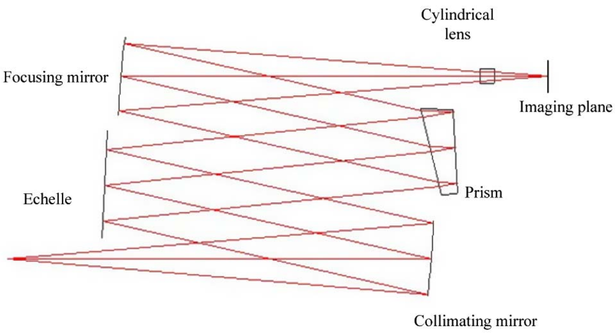

Fig. 1. Optical setup of the échelle spectrometer.

Spherical mirrors are used to collimate and focus the light to reduce complications in instrument adjustments. The symmetric structure (the two spherical mirrors have the same inclination and curvature radius) is designed to eliminate coma [15–18]. For high-grating efficiency [19] and reasonable layout of the optical path, the échelle grating operates subject to the quasi-Littrow condition (whereby the Littrow condition is approximately satisfied, i.e., the grating is rotated a small angle from its Littrow angle). To correct the astigmatism, a cylindrical lens is set in front of the image plane [20–22].

Taking only échelle dispersion into consideration and using the grating equation:

$$m\lambda = d \cdot (\sin \alpha + \sin \beta_\lambda) \cdot \cos \omega, \tag{1}$$

where α is the incident angle, β_λ is the diffraction angle, and ω is the azimuth. Under the quasi-Littrow condition, the reflected angle is equal to the incident angle at the center wavelength of its order. At other wavelengths, $\beta_\lambda - \alpha$ is less than 1.45°, which is why the échelle spectrometer has high dispersion efficiency over the entire spectral range. Hence, we can obtain the correspondence between the diffraction angle and the wavelength.

Generally, there are two options for the prism in the échelle spectrometer: reflecting [23] and transmitting [24]. Although a transmitting prism makes the system compact, we chose a reflecting prism so that the échelle azimuth is constant and the optical structure is symmetric.

Taking only the dispersion from the prism into consideration, the deflection angle Δi between the incident light and the outgoing light of the prism can be expressed as

$$\Delta i = \arcsin\left[n \cdot \sin\left(\theta - \arcsin\left(\frac{\sin i_0}{n}\right)\right)\right] - i_0, \tag{2}$$

where i_0 is the incident angle of the first plane of the prism, and θ is the apex angle of prism. We see from Fig. 1 that if one wavelength satisfies $\Delta i = 2\omega$, the light ray will fall in the center of the image plane. At other wavelengths, $\Delta i - 2\omega$ is less than 1.95°, so the rays fall in a line in the direction of the prism dispersion. As the refractive index is a function of the wavelength, we obtain the corresponding relation between the deflection angle of the prism and the wavelength.

3. SPECTRAL REDUCTION ALGORITHM

Any ray incident on the CCD will be dispersed by the échelle grating and prism. To calculate the correspondence between

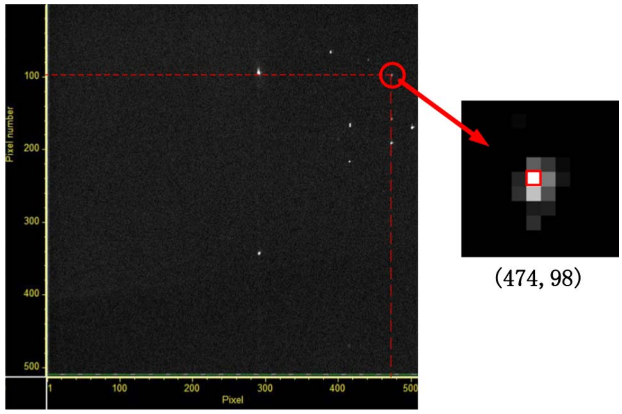

Fig. 2. Coordinates of CCD image plane.

the wavelengths and the pixel position on the CCD, we establish a coordinate system (X, Y) for the image plane (Fig. 2), where X and Y are the pixel addresses in the CCD camera of the corresponding dispersion feature from the échelle grating and prism, respectively. For each light path forming a spot on the CCD image plane, the spectral reduction algorithm establishes a corresponding relation between the wavelength and the spot coordination on the CCD.

As off-axial aberration is unavoidable and complex, the spectral reduction algorithm analyzes only the principal ray. The coordinate of the spot is the same as the coordinate of the pixel that has maximum intensity. The offset distance in the two-dimensional vertical direction from the center of the image plane is calculated in Sections 3.A and 3.B. The compensating error calculated using the algorithm is described in Section 3.C.

A. Direction of Dispersion at the Échelle Grating

To analyze the offset distance in the direction of the échelle grating dispersion (Y), we take a closer look at the focusing mirror. From the model (Fig. 3), the incident plane, outgoing plane, and normal plane are extrapolated out to the same plane, with O being the spherical center of the spherical focus mirror, A the point of origin for the incident light (on the front surface of the échelle grating), D the intersection point of the reflected light and the image plane, and $OH = R$ the radius of the spherical focus mirror. To simplify the calculation, two approximations are introduced (the experiments show that these approximations are within acceptable error ranges):

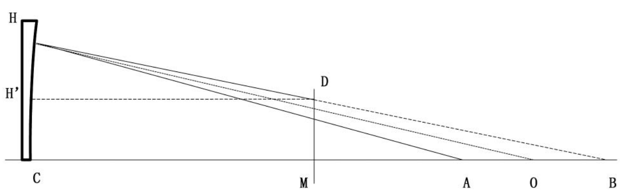

Fig. 3. Modeling the direction of échelle dispersion for a spherical focusing mirror.

(1) As the radius of the spherical focus mirror is much larger than its diameter, HC is approximately perpendicular to OC:

$$DH' = MC = f. \tag{3}$$

(2) With A being the origin point from the échelle grating, AC is the light path from the grating to the spherical focusing mirror. Although the point of origin varies for different wavelengths, the deviation arising from this difference can be neglected. We set AC equal to the distance L from the center of grating to the center of the spherical focus mirror. Therefore, $\angle HAC$ can be written as

$$\angle HAC = \beta_\lambda - \alpha. \tag{4}$$

From the internal angle and exterior angle formulas for the corresponding triangle, we obtain the identities

$$\begin{cases} \angle HAC = \angle AHO + \angle HOC \\ \angle HOC = \angle BHO + \angle HBC \end{cases}. \tag{5}$$

As AH and BH are the incident and reflected light paths, we obtain

$$\angle AHO = \angle BHO. \tag{6}$$

From the two simultaneous equations, Eqs. (5) and (6), $\angle HBC$ is given as

$$\angle HBC = 2\angle HOC - \angle HAC. \tag{7}$$

The offset distance h_y from the center of the image plane in the direction Y can be expressed by

$$\begin{aligned} h_y &= DM \\ &= HC - HH' \\ &= L \cdot \tan(\angle HAC) - f \cdot \tan(\angle HBC). \end{aligned} \tag{8}$$

From Eqs. (4) and (7), we have an expression for $\angle HAC$ and $\angle HBC$ in terms of $\angle HAC$ and $\angle HOC$, which has the expression

$$\angle HOC = \arcsin \frac{HC}{OH} = \arcsin \frac{L \cdot \tan \angle HAC}{R}. \tag{9}$$

By substituting Eqs. (4) and (9) into Eq. (8), h_y can be written as

$$\begin{aligned} h_y &= L \cdot \tan(\beta_\lambda - \alpha) - f \\ &\quad \cdot \tan\left(2 \arcsin \frac{L \cdot \tan(\beta_\lambda - \alpha)}{R} - \beta_\lambda + \alpha\right). \end{aligned} \tag{10}$$

We determine from Eq. (10) that h_y depends only on β_λ. That is, the relationship between the wavelength and coordinate Y is given by Eq. (10). If a cylindrical lens is interposed, the modified geometric model (Fig. 4) yields a correction to Eq. (10).

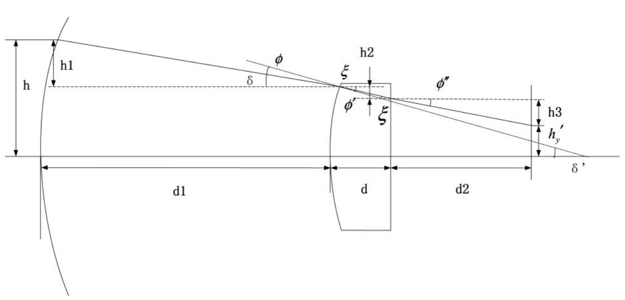

Fig. 4. Modeling the direction of échelle dispersion for a cylindrical lens.

The angle δ in Fig. 4 is the angle $\angle HBC$ in Fig. 3, and δ' is the central angle at the intersection point of the incident light and the front surface of the cylindrical lens. The radius of the front surface of the cylindrical lens is denoted as R'. The actual offset distance h'_y from the center of the image plane in direction Y becomes

$$h'_y = h - h_1 - h_2 - h_3, \tag{11}$$

where h is HC in Fig. 3, which can be calculated using Eq. (8), h_1 and h_2 are the offset distances in direction Y when the light reaches the front and back surfaces, respectively, of the cylindrical lens, and h_3 is the offset distance in direction Y when the light reaches the image plane from the back surface of the lens.

In the approximation, the difference in d_1 at different heights of the cylindrical lens can be ignored, and hence h_1 can be expressed as

$$h_1 = d_1 \cdot \tan \delta. \tag{12}$$

Similarly, the difference in d at different heights of the cylindrical lens can be ignored, and therefore h_2 can be expressed as

$$h_2 = d \cdot \tan \xi. \tag{13}$$

From geometrical considerations and the refraction law,

$$\xi = \delta' - \phi', \tag{14}$$

$$\sin \phi = n \cdot \sin \phi', \tag{15}$$

$$\phi = \delta' - \delta. \tag{16}$$

Substituting Eqs. (14)–(16) into Eq. (13) gives

$$h_2 = d \cdot \tan\left[\delta' - \arcsin\left(\frac{\sin(\delta' - \delta)}{n}\right)\right]. \tag{17}$$

Moreover, h_3 can be expressed as

$$h_3 = d_2 \cdot \tan \phi'', \tag{18}$$

where φ'' is determined from

$$n \cdot \sin \xi = \sin \phi''. \tag{19}$$

By solving the simultaneous equations, Eqs. (17)–(19), h_3 becomes

$$h_3 = d_2 \cdot \tan\left\{\arcsin\left[\sin\left(\delta' - \arcsin\left(\frac{\sin(\delta' - \delta)}{n}\right)\right) \cdot n\right]\right\}. \tag{20}$$

Finally, substituting Eqs. (12), (17), and (20) into Eq. (13), as well as using the expression for $\angle HBC$, h'_y can be rewritten as

$$h_y' = L \cdot \tan(\angle HAC) - d_1 \cdot \tan\delta - d \cdot \tan\left[\delta' - \arcsin\left(\frac{\sin(\delta'-\delta)}{n}\right)\right]$$
$$- d_2 \cdot \tan\left\{\arcsin\left[\sin\left(\delta' - \arcsin\left(\frac{\sin(\delta'-\delta)}{n}\right)\right)\cdot n\right]\right\}$$
$$= L \cdot \tan(\beta_\lambda - \alpha) - d_1 \cdot \tan\left(2\arcsin\frac{L\cdot\tan(\beta_\lambda-\alpha)}{R} - \beta_\lambda + \alpha\right)$$
$$- d \cdot \tan\left[\delta' - \arcsin\left(\frac{\sin\left(\delta' - \left(2\arcsin\frac{L\cdot\tan(\beta_\lambda-\alpha)}{R} - \beta_\lambda + \alpha\right)\right)}{n}\right)\right]$$
$$\times d_2 \cdot \tan\left\{\arcsin\left[\sin\left(\delta' - \arcsin\left(\frac{\sin\left(\delta' - \left(2\arcsin\frac{L\cdot\tan(\beta_\lambda-\alpha)}{R} - \beta_\lambda + \alpha\right)\right)}{n}\right)\right)\cdot n\right]\right\}. \quad \textbf{(21)}$$

We infer from Eq. (21) that h_y' is determined by $\beta_\lambda(\lambda)$ only and thus obtain coordinate Y from h_y'.

B. Direction of Dispersion Toward the Prism

We consider now the focusing mirror to analyze the offset distance (X) for the direction of dispersion at the front surface of the prism. The geometric model for the setup is shown in Fig. 5.

Let O be the center of the spherical focusing mirror, N be the spherical center of the spherical focusing mirror, and HB be the image plane. We have also $\angle OAP = \Delta i - 2\omega$, $ON = PN = R$, and $\angle AON = \angle BON = t$, with R and t already known. To simplify the calculation, we introduce three approximations (the experiments show that these approximations are within acceptable error ranges):

(1) A is the origin point of the prism and AC is the light path from the prism to the spherical focus mirror. Although the points of origin vary with the wavelength, the differences can be neglected and hence AC approximately equals the distance L' from the center of the prism to the center of the spherical focus mirror.

(2) As the radius of the spherical focus mirror is much larger than its diameter, OP is an adjacent of the approximately right-angled triangles ΔAOP, ΔNOP, and ΔBOP, from which we can derive:

$$OA \cdot \tan\angle OAP = ON \cdot \tan\angle ONP = OB \cdot \tan\angle OBP, \quad \textbf{(22)}$$

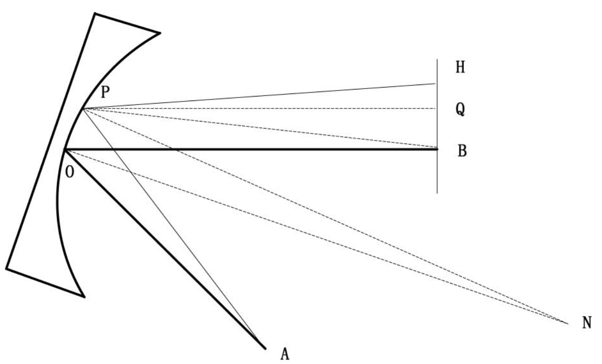

Fig. 5. Modeling of the direction of dispersion from the spherical focusing mirror onto the prism.

$$\begin{cases} \angle ONP = \arctan\left(\frac{L'\cdot\tan(\Delta i - 2\omega)}{R}\right) \\ \angle OBP = \arctan\left(\frac{f\cdot\tan(\Delta i - 2\omega)}{R}\right) \end{cases}. \quad \textbf{(23)}$$

(3) As the radius of the spherical focus mirror is much larger than its diameter, then we have approximately $PQ = OB = f$.

From geometric identities and the internal angle relations of the triangle, we can derive:

$$\begin{cases} \angle AON = \angle BON \\ \angle APN = \angle HPN \\ \angle HPN = \angle HPQ + \angle QPB + \angle BPN \\ \angle AON + \angle OAP = \angle APN + \angle PNO \\ \angle OAP + \angle AOB = \angle APB + \angle PBO \end{cases}. \quad \textbf{(24)}$$

From Eqs. (23) and (24), $\angle HPQ$ can be expressed as

$$\angle HPQ = \angle OAP - 2\angle OBP + 2\angle AON$$
$$= \Delta i - 2\omega - 2\arctan\left(\frac{f\cdot\tan(\Delta i - 2\omega)}{R}\right) + 2t. \quad \textbf{(25)}$$

The offset distance h_x from the center of the image plane at the direction of prism dispersion can be expressed as

$$h_x = QB + HQ. \quad \textbf{(26)}$$

With $\angle OAP = \Delta i - 2\omega$, QB becomes

$$QB = OP$$
$$= L' \cdot \angle OAP$$
$$= L' \cdot \tan(\Delta i - 2\omega). \quad \textbf{(27)}$$

Using Eq. (25), HQ can be expressed as

$$HQ = f \cdot \angle HPQ$$
$$= f \cdot \tan\left[\Delta i - 2\omega - 2\arctan\left(\frac{f\cdot\tan(\Delta i - 2\omega)}{R}\right) + 2t\right]. \quad \textbf{(28)}$$

By substituting Eqs. (27) and (28) into Eq. (26), h_x can be written as follows:

$$h_x = L' \cdot \tan(\Delta i - 2\omega) + f \cdot \tan\left[\Delta i - 2\omega - 2\arctan\left(\frac{f \cdot \tan(\Delta i - 2\omega)}{R}\right) + 2t\right]. \quad (29)$$

We determine from Eq. (29) that h_x depends only on Δi. That is, the relationship between the wavelength and coordinate X is given by Eq. (29). For a cylindrical lens, we establish the geometric model (see Fig. 6) to provide the correction for Eq. (29).

Suppose that the cylindrical lens is a parallel plate in the direction of X, with the thickness of the plate being d. The offset distance $\Delta h = HH'$ caused by the cylindrical lens can be expressed as

$$\Delta h = d \cdot (\tan i_i - \tan i_i'), \quad (30)$$

where i_i is $\angle HPQ$, which is the incident angle of the cylindrical lens, and i_i' is the refraction angle. The angles i_i and i_i' satisfy the refraction law:

$$\sin i_i = n \cdot \sin i_i'. \quad (31)$$

From the simultaneous equations of Eqs. (30) and (31) and from $\angle HPQ, h = HH'$ can be rewritten as

$$\Delta h = d \cdot \left\{ \tan\left[\Delta i - 2\omega - 2\arctan\left(\frac{f \cdot \tan(\Delta i - 2\omega)}{R} + 2t\right)\right] - \tan\left[\arcsin\frac{\sin\left(\Delta i - 2\omega - 2\arctan\left(\frac{f \cdot \tan(\Delta i - 2\omega)}{R} + 2t\right)\right)}{n}\right]\right\}. \quad (32)$$

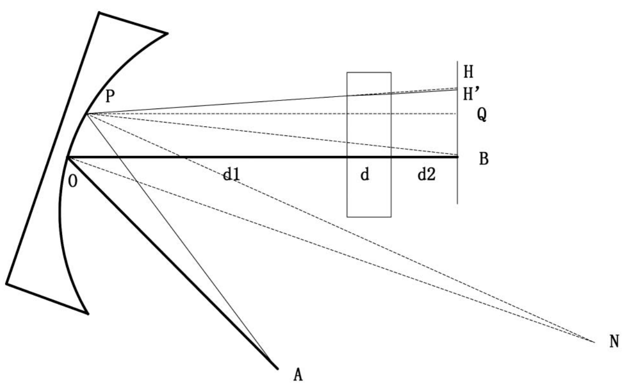

Fig. 6. Modeling the direction of dispersion from the prism to the cylindrical lens.

Finally, h_x' can be rewritten as

$$\begin{aligned} h_x' &= h_x - \Delta h \\ &= L' \cdot \tan(\Delta i - 2\omega) \\ &\quad + f \cdot \tan\left[\Delta i - 2\omega - 2\arctan\left(\frac{f \cdot \tan(\Delta i - 2\omega)}{R}\right) + 2t\right] \\ &\quad - d \cdot \left\{ \tan\left[\Delta i - 2\omega - 2\arctan\left(\frac{f \cdot \tan(\Delta i - 2\omega)}{R}\right) + 2t\right] \right. \\ &\quad \left. - \tan\left[\arcsin\frac{\sin\left(\Delta i - 2\omega - 2\arctan\left(\frac{f \cdot \tan(\Delta i - 2\omega)}{R} + 2t\right)\right)}{n}\right]\right\}. \end{aligned} \quad (33)$$

We deduce from Eq. (33) that h_x' is determined by $\Delta i(\lambda)$ only and obtain coordinate X from h_x'.

C. Optimization Algorithm of Spectral Reduction Algorithm

Recalling the algorithm for spectral reduction discussed earlier, a spectral reduction model can be established. The relationship between the wavelength and the spot coordinate can be determined using the model. The model generates a matrix that corresponds to the CCD array, and its elements are wavelengths. The accuracy criterion is that the largest deviation is no more than one pixel.

However, the model still has deviations in the direction of X and the largest deviation is more than one pixel, assuming that the deviation in direction X is solely caused by the spectral line bending of the reflecting prism [25,26]. To compensate the influence of the spectral line bending of the reflecting prism on coordinate X, we developed a geometric model (see Fig. 7). Since the spectral line bending is difficult to express by equations, we analyze the spectral line bending by vector.

A rectangular coordinate system is established with the origin of the coordinate system set at the center of the front surface of the prism. AO is the incident light ray into the principal section, and BO is the incident light ray out of the principal section, which satisfied $\angle AOB = \beta_\lambda - \alpha$. The incident angle i_0 of the prism is $\angle AOX$. To get the angular information only, we

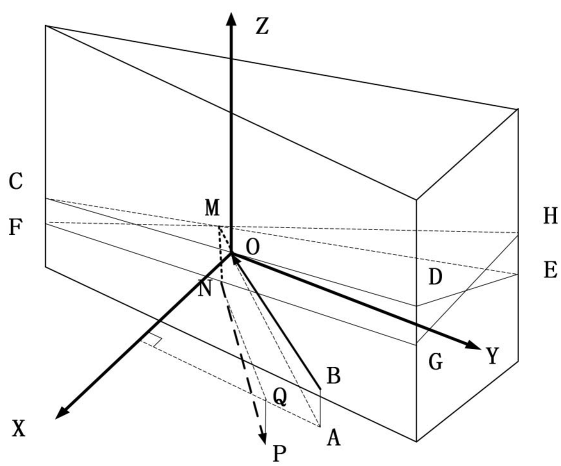

Fig. 7. Geometric model of the prism.

set the incident light unit length and calculate the coordinate of the outgoing light ray to get the angular deviation.

As the information of the incident light is known, we can obtain the information of the refracting ray and the reflecting ray by the steps below:

(1) Depending on the directional vector of the incident ray and the normal vector at the incident point, the plane determined by the incident light and the normal can be calculated.

(2) Depending on the coordinates of the prism, the coordinates of the triangle determined by the prism and the plane determined by step 1 can be calculated.

(3) From the law of reflection and the law of refraction, the vector of the reflected ray and refracted ray in the triangle by step 2 can be calculated.

Using these three steps, we calculate the vectors BO, OM, MN, and NP one by one. Finally, according to the vector coordinate of NP, we obtain the angular deviation in direction X. NP can be expressed as a function of $\beta_\lambda - \alpha$, and therefore we obtain the corrected X by substituting the angular deviation in direction X into Eq. (33).

4. EXPERIMENTAL RESULTS AND DISCUSSION

We chose the échelle spectrometer developed by our team for the experiment and constructed the model matrix to get the wavelength using the spot coordinates on the CCD. The parameters of the échelle spectrometer related to the model are shown in Table 1.

At the same time, we used ray-tracing software to verify the accuracy of the model, regarding the trace results as the actual coordinates. We refer to this algorithm that compensates for spectral line bending as the "optimized spectra reduction." The contrast results are shown in Table 2.

As the influences of aberrations and spectral line bending are greater at the edge of the image plane, we chose nine wavelengths that fall in the middle and on the edge and corner of the CCD to obtain a wide range of data. We can determine that:

(1) By comparing columns 3 and 4, the coordinate deviation of the spectra reduction is more than one pixel on the right edge of the CCD image, and the closer the spot is to the edge of the CCD image, the bigger the coordinate deviation is.

Table 1. Parameters of Échelle Spectrometer

Parameters	Value
Focus length	262 mm
Groove density of échelle	54.5 gr/mm
Incident angel of échelle	46°
Azimuth of échelle	8°
Incident angel of prism	10.44°
Apex angle of prism	12°
Radius of the spherical focus mirror	520.9 mm
Radius of front surface of the cylindrical lens	180.5 mm
Thickness of cylindrical lens	9 mm
Diameter of pin hole	25 μm
Pixel size	26 μm

Table 2. Contrast Table for the Spot Coordinate

Wavelength	Order	Coordinate of Ray Tracing	Coordinate of Spectral Reduction	Coordinate of Optimized Spectral Reduction
188.919	140	(4.7, 40.6)	(5, 40)	(4, 40)
189.427	138	(9.6, 256)	(9, 256)	(9, 256)
189.899	136	(11.9, 470.6)	(12, 471)	(11, 471)
242.682	109	(256.3, 35.4)	(257, 35)	(256, 35)
242.045	108	(256.4, 256)	(256, 256)	(256, 256)
241.344	107	(252.5, 474.8)	(254, 475)	(252, 475)
575.131	46	(499.3, 30.1)	(501, 29)	(500, 29)
580.909	45	(501.2, 256)	(502, 256)	(502, 256)
586.876	44	(501.1, 478.3)	(503, 479)	(501, 479)

(2) Comparing columns 3 and 5, the coordinate deviation of the optimized spectral reduction over the whole image plane is less than one pixel.

To establish whether the deviation is caused by the spectral line bending of the prism, we chose wavelengths of the order 46, which fall on the right side of the CCD image, for analysis. The simulation results shows that the ray tracing has the same tendency as the spectral line bending and the coordinate, for the optimized spectral reduction is closer to that for ray tracing than for spectral reduction (see Fig. 8).

As the characteristic wavelength of mercury is known, we captured mercury's spectral image using the CCD (see Fig. 9) to test the accuracy of the optimized spectra reduction algorithm. The contrast results are shown in Table 3.

Choosing the eight characteristic wavelengths of mercury for analysis, we determined that:

(1) By comparing columns 3 and 4, the coordinate deviation between the ray tracing and the CCD is less than one pixel, the deviation being the result of the adjustment error.

(2) By comparing columns 4 and 5, the coordinate deviation between the CCD and spectra reduction is less than

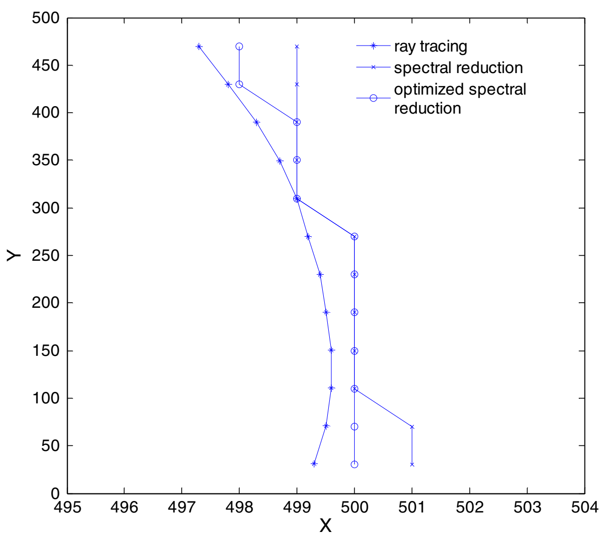

Fig. 8. Coordinate contrast.

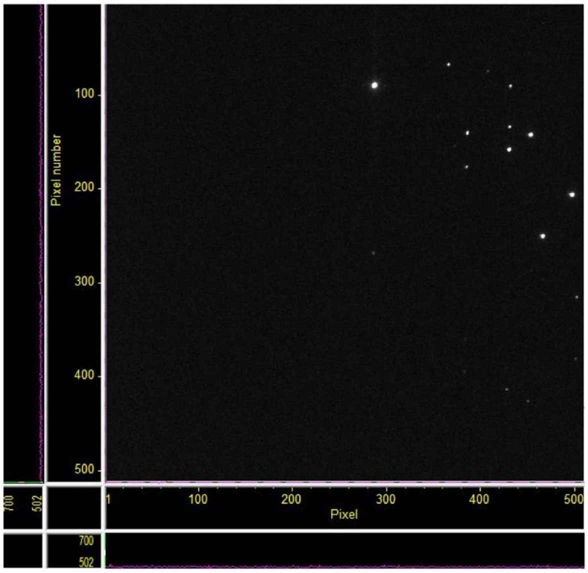

Fig. 9. Spectral image of mercury.

Table 3. Contrast Table for the Coordinate Spots from a Mercury Lamp

Wavelength	Order	Coordinate of Ray Tracing	Coordinate of CCD	Coordinate of Optimized Spectral Reduction
253.652	103	(285.6, 87.1)	(286, 88)	(286, 88)
296.728	89	(364.4, 65.6)	(364, 66)	(365, 66)
313.184	84	(385.5, 138.1)	(385, 138)	(386, 138)
404.656	65	(453.8, 141.1)	(453, 141)	(454, 141)
435.834	60	(466.9, 249.5)	(466, 250)	(467, 249)
546.075	48	(495.5, 205.9)	(497, 205)	(496, 205)
576.961	45	(500.3, 380.7)	(501, 380)	(501, 381)
579.017	45	(500.9, 316)	(502, 316)	(501, 316)

one pixel, which means the algorithm fulfills the resolution requirements of the échelle spectrometer.

5. CONCLUSIONS

The spectral reduction algorithm, which constructs a mathematical model by calculating the offset distance of the principal ray, is improved. We have shown both numerically and experimentally that the spot coordinates of any wavelength can be calculated quickly by the model, which is suitable for an échelle spectrometer with spherical mirrors in accordance with the known design parameters. To improve the accuracy of the algorithm, the spectral line bending of the reflecting prism was taken into consideration to compensate for the algorithm's error. The experiment showed that the error for the algorithm model is less than one pixel over the whole CCD image plane, which takes full advantage of the high spectral resolution of the échelle spectrometer.

Funding. Chinese Finance Ministry for the National R&D Projects for Key Scientific Instruments (ZDYZ2008-1); National Natural Science Foundation of China (NSFC) (61505204); National Ministry of Science and Technology for National Key Basic Research Program of China (2014CB049500); National Key Scientific Instrument and Equipment Development Projects in China (2014YQ120351).

REFERENCES

1. H. Becker-Ross, M. Okruss, S. Florek, U. Heitmann, and M. D. Huang, "Echelle-spectrograph as a tool for studies of structured background in flame atomic absorption spectrometry," Spectrochim. Acta Part B **57**, 1493–1504 (2002).
2. L. Xu, M. A. Davonport, M. A. Turner, T. Sun, and K. F. Kelly, "Compressive Echelle spectroscopy," Proc. SPIE **8165**, 81650E (2011).
3. N. E. Piskunov and J. A. Valenti, "New algorithms for reducing cross-dispersed echelle spectra," Astron. Astrophys. **385**, 1095–1106 (2002).
4. P. Xie, Z. Ni, Y. Huang, D. Zhang, and Y. Zhang, "Application research progress in the echelle grating," Laser J. **30**, 4–6 (2009).
5. X. Wu, Y. Zhu, and L. Wang, "Optical design of high resolution echelle spectrograph," Opt. Precis. Eng. **11**, 442–447 (2003).
6. G. R. Harrison, "The production of diffraction gratings I. Development of the ruling art," J. Opt. Soc. Am. **39**, 413–426 (1949).
7. J.-F. Lavigne, M. Doucet, M. Wang, J. Lacoursière, M. Grill, R. Melchiorri, T. G. Slanger, and E. Kendall, "Study of the image quality and stray light in the critical design phase of the compact Echelle spectrograph for aeronomical research (CESAR)," Proc. SPIE **7735**, 773539 (2010).
8. C. Vannahme, M. Dufva, and A. Kristensen, "High frame rate multi-resonance imaging refractometry with distributed feedback dye laser sensor," Light Sci. Appl. **4**, e269 (2015).
9. P. Ballester and M. R. Rosa, "Modeling echelle spectrographs," Astron. Astrophys. Suppl. Ser. **126**, 563–571 (1997).
10. J. J. McNeill, "Wavelength measurement in echelle spectra," J. Opt. Soc. Am. **49**, 441–444 (1959).
11. N. A. Finkeilstein, "The measurement of wavelength in echelle spectra," J. Opt. Soc. Am. **43**, 90–96 (1953).
12. S. Chen, Y. Tang, Bayanheshig, X. Qi, and W. Zhu, "A new type of wide spectral coverage echelle spectrometer design for ICP-AES," Proc. SPIE **8557**, 85571M (2012).
13. Y. Tang, S. Chen, Bayanheshig, J. Cui, and J. Chen, "Spectral reducing of cross-dispersed echelle spectrograph and its wavelength calibration," Opt. Precis. Eng. **18**, 2130–2136 (2010).
14. A. A. Dantzler, "Echelle spectrograph software design aid," Appl. Opt. **24**, 4504–4508 (1985).
15. C. D. Allemand, "Coma correction in Czerny–Turner spectrographs," J. Opt. Soc. Am. **58**, 159–163 (1968).
16. J. N. Howard, "Coma correction for a Czerny–Turner monochromator: comment," Appl. Opt. **21**, 1708 (1982).
17. M. A. Gil, J. M. Simon, and A. N. Fantino, "Czerny–Turner spectrograph with a wide spectral range," Appl. Opt. **27**, 4069–4072 (1988).
18. K.-S. Lee, K. P. Thompson, and J. P. Rolland, "Broadband astigmastism-corrected Czerny–Turner spectrometer," Opt. Express **18**, 23378–23384 (2010).
19. A. T. Zander, M. H. Miller, M. S. Hendrick, and D. Eastwood, "Spectral efficiency of spectraspan III echelle grating spectrometer," Appl. Spectrosc. **39**, 1–5 (1985).
20. Z. Ma, X. Qi, X. Li, S. Zhang, Bayanheshig, H. Yu, H. Yu, and Q. Jiao, "New measuring method of diffraction efficiency for plane grating based on Fourier spectral technology," Appl. Opt. **55**, 522–558 (2016).
21. Y. Tang, C. Zheng, Y. Nan, F. Li, and L. Guo, "Study of anamorphose correction of astigmatism-corrected Czerny–Turner imaging spectrometer," Acta Opt. Sin. **35**, 0112007 (2015).

22. L. Yan, “Study on the advanced Czerny–Turner imaging spectrometer with high resolution in broadband,” Spectrosc. Spect. Anal. **35**, 1756–1760 (2015).
23. S. Florek, C. Haisch, M. Okruss, and H. Becker-Ross, “A new, versatile echelle spectrometer relevant to laser induced plasma applications,” Spectrochim. Acta Part B **56**, 1027–1034 (2001).
24. J. Koch, M. Okruss, J. Franzke, S. V. Florek, K. Niemax, and H. Becker-Ross, “Element-selective detection of gas chromatographic eluates by near infrared echelle optical emission spectrometry on microwave-induced plasmas,” Spectrochim. Acta Part B **59**, 199–207 (2004).
25. Y. Chen, Y. Ji, J. Zhou, X. Chen, X. Wei, and W. Shen, “Wavelength calibration and spectral line bending determination of an imaging spectrometer,” Proc. SPIE **7384**, 73841G (2009).
26. L. Qian, L. Xiang, Q. Lv, and W. Huang, “Analysis and simulation of effect of spectral line bending on computational imaging spectrometry,” Acta Photon. Sin. **42**, 897–901 (2013).